Published on 07 November 2016. Downloaded by University of Science and Technology of China on 14/06/2017 03:17:43.

Nanoscale

PAPER

View Article Online
View Journal | View Issue

Cite this: *Nanoscale*, 2016, **8**, 19761

Enhanced CO oxidation on CeO_2/Co_3O_4 nanojunctions derived from annealing of metal organic frameworks†

Changlai Wang,[a] Dongdong Wang,[a] Yang Yang,[a] Ren Li,[a] Changle Chen*[b] and Qianwang Chen*[a,c]

Received 30th September 2016,
Accepted 4th November 2016

DOI: 10.1039/c6nr07725k

www.rsc.org/nanoscale

The interface of nanojunctions plays an important role in the performance of heterogeneous catalysts. However, it is highly challenging to construct nanojunctions which are usually prepared by complex multi-step processes. Metal–organic frameworks (MOFs), with designable metal centers and tunable organic ligands, are promising precursors for the one-step synthesis of nanojunctions. Herein, we prepared porous CeO_2/Co_3O_4 nanojunctions by direct annealing of MOFs in air. These unique nanojunctions exhibit remarkable catalytic activity for CO oxidation, which can achieve complete oxidization of CO to CO_2 at 110 °C. In contrast, the temperature required for 100% CO oxidation is 190 °C for pure Co_3O_4. Moreover, the nanojunctions can maintain complete CO conversion after 16 h at 110 °C. Density functional theory calculations revealed that the enhancement in the catalytic activity of CeO_2/Co_3O_4 nanojunctions can be attributed to the charge transfer through the interfaces of the nanojunctions.

Introduction

The catalytic oxidation of CO has attracted considerable attention in the energy and environmental fields, as it shows strong potential not only for clean energy conversion in proton exchange membrane fuel cells, but also for environmental pollution issues, especially in the control of automobile exhausts.[1–4] Catalysts based on noble metals are most efficient for CO oxidation.[5–9] However, the sensitivity of precious metals to sulfur poisoning and their high cost hinder their further applicability.[10,11] As a result, it is highly urgent and necessary to explore alternatives with low cost and high stability.

Recently, theoretical and experimental results indicated that transition-metal oxides and their mixed oxides are promising candidates for CO oxidation.[12,13] For example, Wang *et al.* suggested that Co_3O_4 could possess high catalytic activity for CO oxidation based on density functional theory calculations.[14] The rattle-type Co_3O_4@SiO_2 nanoparticles synthesized by our group through thermal decomposition of $Co_3[Co(CN)_6]_2$@SiO_2 core–shell nanocubes exhibited excellent catalytic performance for CO oxidation.[15] Li *et al.* synthesized ceria nanorods with rich oxygen vacancies by a hydrothermal method, which also showed outstanding catalytic activity toward CO oxidation.[16] Compared with single-component structures, multi-component hybrid structures usually exhibit enhanced catalytic performance as they have some additional effects such as the synergistic effect[17] and the interfacial effect.

The interfacial effect plays an essential role in catalytic oxidation performance for heterogeneous catalysis. The exposed interfaces can serve as the catalytic active sites as they render hybrid junctions with rich redox reactions. Bao *et al.* showed that the interface-confined coordinatively unsaturated ferrous sites between Pt and nano-FeO_{1-x} were the active center for the activation of O_2.[18] Zheng *et al.* reported that the OH groups at the Fe^{3+}–OH–Pt interfaces readily react with the CO adsorbed nearby to yield CO_2 and simultaneously produce coordinatively unsaturated Fe sites for O_2 activation.[19] In addition, adsorbents, charges and intermediates are usually transferred at the interfaces during catalytic reactions. Xiong *et al.* found that interface polarization drove the charge transfer from Ag to CuO, leading to the enhancement of CO oxidation.[20] However, most interfaces in core–shell structures are usually not catalytic active sites due to their thick shells which hinder the direct contact between CO and catalysts. Apart from this, the precisely controlled synthesis of interface structures is

[a]*Department of Materials Science & Engineering, Hefei National Laboratory for Physical Science at Microscale & Collaborative Innovation Center of Suzhou Nano Science and Technology, University of Science and Technology of China, Hefei 230026, China. E-mail: cqw@ustc.edu.cn*
[b]*Department of Polymer Science & Engineering, University of Science and Technology of China, Hefei 230031, China. E-mail: changle@ustc.edu.cn*
[c]*High Magnetic Field Laboratory, Hefei Institutes of Physical Science, Chinese Academy of Sciences, Hefei 230031, China*

†Electronic supplementary information (ESI) available. See DOI: 10.1039/c6nr07725k

Published on 07 November 2016. Downloaded by University of Science and Technology of China on 14/06/2017 03:17:43.

rather rare and usually associated with complicated processes,[21] thus the development of efficient strategies could be highly beneficial for the design of high performance heterogeneous catalysts.

Over the past few decades, metal–organic frameworks (MOFs) have exhibited great potential as effective sacrificial templates or reactive precursors to construct various nanostructures due to their open channels, permanent cavities, and high surface areas.[22–25] Since the first report on nanoporous carbon materials by Xu *et al.* using MOF-5 as the template and furfuryl alcohol (FA) as the carbon precursor,[26] several types of derivatives have been prepared by carbonization of MOFs. For example, Yamauchi *et al.* synthesized nanoporous carbon particles with magnetic Co nanoparticles through pyrolysis of Co-containing MOFs (ZIF-67) under an atmosphere of nitrogen.[27] Lou *et al.* prepared Fe_2O_3 microboxes with iron-based MOFs ($Fe_4[Fe(CN)_6]_3$) as the precursor.[28] Our group has found that MOFs can be used as templates to fabricate various nanomaterials,[29–32] including various metal oxides and their composite materials. It is possible to obtain the desired nanoarchitectures by selecting suitable MOFs with special morphologies and appropriate experimental conditions.

We hypothesized that the combination of Prussian blue analogues (PBA), transition metals or rare earth metals as metallic nodes, and –C≡N groups as linkers, could provide an ideal precursor for the fabrication of non-precious metal oxide nanojunctions. In this contribution, we developed a novel *in situ* synthetic strategy to fabricate CeO_2/Co_3O_4 nanojunctions by directly annealing the preformed $Ce[Co(CN)_6]$ in air. The unique nanojunctions possess numerous interfaces due to the uniformly dispersed CeO_2 and Co_3O_4 nanocrystals during the annealing process. In addition, the nanojunctions prepared using this strategy possess high specific surface areas and a large number of nanopores as gaseous molecules are released through MOF pyrolysis. The catalytic oxidation of CO was chosen as the model reaction to study the catalytic properties of the nanojunctions. For comparison, we also evaluated the catalytic performance of pure Co_3O_4 for CO oxidation. Density functional theory calculations were performed to probe the mechanistic aspects of the nanojunctions. This study will provide a universal strategy to prepare nanojunctions and to gain better understanding of the influence of nanojuctions on catalytic performance.

Experimental

Synthesis of catalysts

The hexagonal nanosheet $Ce[Co(CN)_6]$ precursor was synthesized by the following procedure: Solution A: 0.1 mmol $Ce(NO_3)_3$ and 0.3 g PVP surfactant were dissolved in 10 mL H_2O and 20 mL C_2H_5OH under agitated stirring, Solution B: 0.05 mmol $K_3[Co(CN)_6]_2$ was dissolved in 10 mL H_2O and 20 mL C_2H_5OH under agitated stirring. Solution B was slowly and regularly added to Solution A through a syringe. The whole reaction was performed at room temperature with agitated stirring. After 10 min, the reaction was aged for 24 h at room temperature without any interruption. The resulting white precipitate was isolated by filtration, washed several times with absolute ethanol, and finally dried in an oven at 60 °C. Porous CeO_2/Co_3O_4 nanojunctions were successfully obtained by the thermal decomposition of $Ce[Co(CN)_6]$ at 600 °C for 3 h with a temperature ramp of 5 °C min^{-1} in air.

Material characterization

The powder X-ray diffraction (XRD) patterns of the samples were collected from a Japan Rigaku D/MAX-γA X-ray diffractometer equipped with Cu Kα radiation. The average particle size of the samples was evaluated from X-ray line broadening analysis using the well-known Scherer equation ($d = 0.89k/\beta b \cos\theta$). Field emission scanning electron microscopy (FESEM) images were recorded on a JEOLJSM-6700 M scanning electron microscope. Transmission electron microscopy (TEM) images were recorded with a Hitachi H-800 transmission electron microscope using an accelerating voltage of 200 kV, and a high resolution transmission electron microscope (HRTEM) (JEOL-2011) was operated at an acceleration voltage of 200 kV. The specific surface area was evaluated at 77 K (Micromeritics ASAP 2020) using the Brunauer–Emmett–Teller (BET) method, while the pore volume and pore size were calculated according to the Barrett–Joyner–Halenda (BJH) formula applied to the adsorption branch. Thermogravimetric analysis (TGA) was carried out using a Shimadzu-50 thermoanalyser under air flow. X-ray photoelectron spectroscopy (XPS) was performed on a VGESCALAB MKII X-ray photoelectron spectrometer using an Al Kα excitation source. The FTIR spectrum was determined using a Magna-IR 750 spectrometer.

Catalytic performance measurements

The catalytic activity of CeO_2/Co_3O_4 for the oxidation of CO was carried out using a fixed-bed flow reactor. For a typical measurement, 50 mg of catalyst was loaded into the reactor. And the reaction gas consisting of 1% CO and 99% dry air was fed at a rate of 30 mL min^{-1}. The catalyst was heated to the desired reaction temperature at a rate of 2 °C min^{-1} and then maintained there for 30 min until the catalytic reaction reached a steady state. Then the composition of effluent gas was analyzed with an online GC-14B gas chromatograph. The conversion of CO was calculated from the change in the CO concentration of the inlet and outlet gases.

Results and discussion

As illustrated in Scheme 1, the hexagonal nanosheet $Ce[Co(CN)_6]$ was synthesized at room temperature and then it was designed as a self-sacrificing template to fabricate CeO_2/Co_3O_4 nanojunctions. $Ce[Co(CN)_6]$, with –C≡N groups as linkers, and transition metal Co and rare earth metal Ce as metallic nodes, which has two different kinds of metals, behaves an ideal precursor for the preparation of nanojuctions. During the annealing process in air, Ce and Co

 This journal is © The Royal Society of Chemistry 2016

Published on 07 November 2016. Downloaded by University of Science and Technology of China on 14/06/2017 03:17:43.

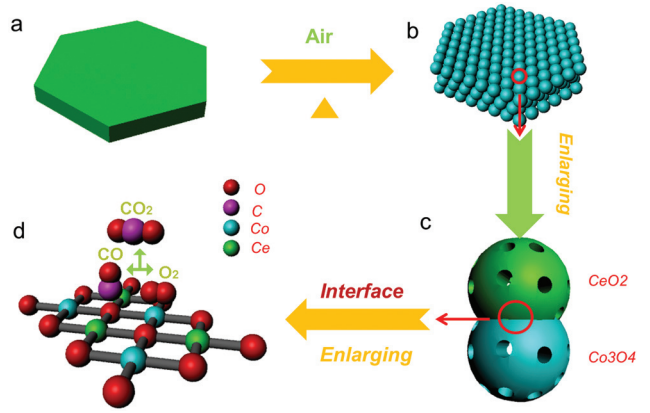

Scheme 1 Schematic illustration of the synthesis procedure of porous CeO_2/Co_3O_4 nanojunctions. (a) Hexagonal sheet MOFs named $Ce[Co(CN)_6]$. (b) Porous CeO_2/Co_3O_4 nanojunctions. (c) Enlarged porous CeO_2/Co_3O_4 nanojunctions. (d) CO oxidation over the interface between CeO_2 and Co_3O_4.

atoms from the precursor will form CeO_2 and Co_3O_4 nanoparticles, meanwhile interfaces between CeO_2 and Co_3O_4 will *in situ* be generated. The *in situ* formed interfaces play a vital role in CO catalytic oxidation. Moreover, with the release of gaseous molecules (*e.g.* CO_2 and H_2O) during the annealing process, a large number of nanopores will be formed in CeO_2/Co_3O_4 nanojunctions. And these nanopores can offer paths for gas diffusion, which is beneficial to the catalytic reaction as well.

As revealed by the scanning electron microscopy image (SEM) in Fig. 1a, a uniform hexagonal nanosheet precursor with an edge of about 1 μm has been prepared. Powder X-ray diffraction (as shown in Fig. S1, ESI†) was also used to characterize the structure of the as-prepared precursor, and the result confirmed the successful synthesis of the targeted $Ce[Co(CN)_6]$, according to the result reported by Mullica's group.[33] The thermogravimetric analysis (TGA) of $Ce[Co(CN)_6]$ is shown in Fig. S2.† The first step shows a significant weight loss of 16.78% between room temperature and 250 °C illustrating the loss of water molecules from the porous framework of $Ce[Co(CN)_6]$. When the temperature is further increased to 400 °C, a second weight loss of 24.18% is observed between 250 °C and 400 °C due to the oxidation of the cyanide and residual surfactant. Based on the TGA results, a temperature of 600 °C was chosen as the calcination temperature for porous CeO_2/Co_3O_4 nanojunctions. The MOF precursor has been totally decomposed at this temperature, which can be seen from the FTIR spectrum of the CeO_2/Co_3O_4 nanojunctions (Fig. S3†).

The conversion of $Ce[Co(CN)_6]$ to porous CeO_2/Co_3O_4 nanojunctions was investigated by transmission electron microscopy (TEM). As we can see from Fig. 1b, the resulting product inherits the hexagonal morphology, and the ultrafine CeO_2/Co_3O_4 nanocrystals are distributed homogenously in a hexagonal nanosheet structure. The high-resolution transmission electron microscopy (HRTEM) image of porous CeO_2/Co_3O_4 nanojunctions is shown in Fig. 1c and more HRTEM images can be seen in Fig. S4.† The measured interlayer distance of 0.313 nm is consistent with the (111) planes of CeO_2, while the interlayer distance of 0.285 nm agrees with the (220) planes of Co_3O_4, respectively. It is worth noting that the white circle marked in Fig. 1c reveals the interfaces between the

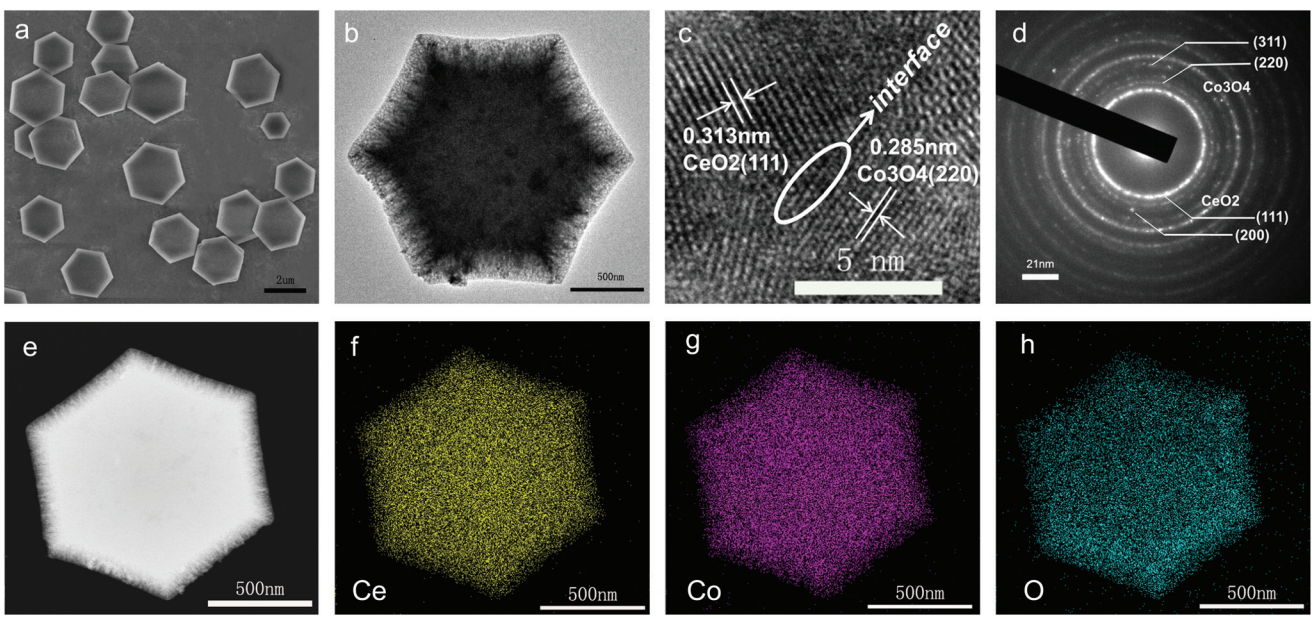

Fig. 1 (a) FESEM image of the as-prepared $Ce[Co(CN)_6]$ precursor, (b) TEM image, (c) HRTEM images of the porous CeO_2/Co_3O_4 nanojunctions, (d) selected area electron diffraction pattern of porous CeO_2/Co_3O_4 nanojunctions, (e) scanning TEM image of porous CeO_2/Co_3O_4 nanojunctions, (f–h) energy dispersive X-ray spectrometry elemental maps of Ce, Co, and O, respectively.

Published on 07 November 2016. Downloaded by University of Science and Technology of China on 14/06/2017 03:17:43.

CeO_2 nanocrystal and the Co_3O_4 nanocrystal, indicating the generation of nanojunctions composed of CeO_2 and Co_3O_4. The corresponding selected area electron diffraction (SAED) pattern (Fig. 1d) shows many spotty ring patterns of CeO_2 and Co_3O_4 phases, indicating that there are a large number of nanojunctions in our prepared materials. The scanning TEM image of porous CeO_2/Co_3O_4 nanojunctions is shown in Fig. 1e. It is clear that the nanojunctions display a hexagonal nanosheet structure. As shown in Fig. 1f–h, the energy dispersive X-ray spectrometry elemental maps reveal that the Ce, Co and O elements are uniformly distributed in the hexagonal nanosheet structure, indicating that CeO_2 and Co_3O_4 nanocrystals are uniformly dispersed in the MOF structure, which further confirms the interface structure of CeO_2/Co_3O_4 nanojunctions.

The X-ray diffraction pattern (Fig. 2a) of the nanojunctions shows that all the diffraction peaks can be assigned to the cubic fluorite phase CeO_2 (JCPDS 34-0394) and the fcc phase Co_3O_4 (JCPDS 74-1657). No additional impurity peaks can be seen, implying the high purity of the product. The broadening of the diffraction peaks is attributed to the small CeO_2 and Co_3O_4 crystal particles. The average grain sizes of CeO_2 and Co_3O_4 powders are approximately 9.4 and 10.5 nm as determined by the Scherrer equation, respectively. Energy-dispersive X-ray spectroscopy (EDS) indicates the existence of Ce, Co and O (Fig. 2b), and C and Cu are from the background.

In order to investigate the surface composition and chemical state of the porous CeO_2/Co_3O_4 nanojunctions, X-ray photoelectron spectroscopy (XPS) characterization was carried out, and the results are shown in Fig. 3 and S5.† The XPS spectrum of O 1s is deconvolved into two peaks in Fig. 3a. The peak centered at 529.3 eV stands for the surface lattice oxygen in the metal oxides. The other peak located at 531.4 eV is ascribed to the oxygen in hydroxyl groups.[34,35] Fig. 3b shows the Ce 3d XPS spectrum, which can be deconvolved into eight peaks. The peaks labeled as M_1 and N_1 are the characteristic peaks of Ce(III) states, while others are the characteristic peaks of Ce(IV) states.[36] Fig. 3c displays the Co 2p XPS spectrum, which shows two major peaks with binding energies at 779.5 and 794.6 eV, corresponding to Co 2p 3/2 and Co 2p1/2. Compared with pure Co_3O_4 (Fig. S9†), the Co 2p peaks of porous CeO_2/Co_3O_4 nanojunctions shift to lower binding energies. This phenomenon could be attributed to the charge transfer from Ce to the far more electrophilic Co, indicating that there is a strong interaction between CeO_2 and Co_3O_4 in porous CeO_2/Co_3O_4 nano-

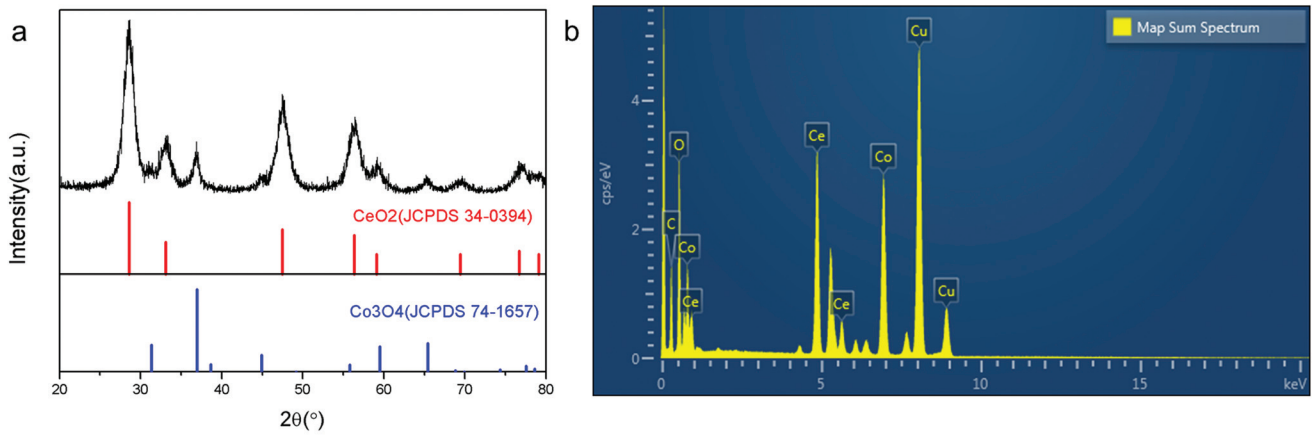

Fig. 2 (a) XRD patterns of porous CeO_2/Co_3O_4 nanojunctions, (b) EDS spectrum of porous CeO_2/Co_3O_4 nanojunctions.

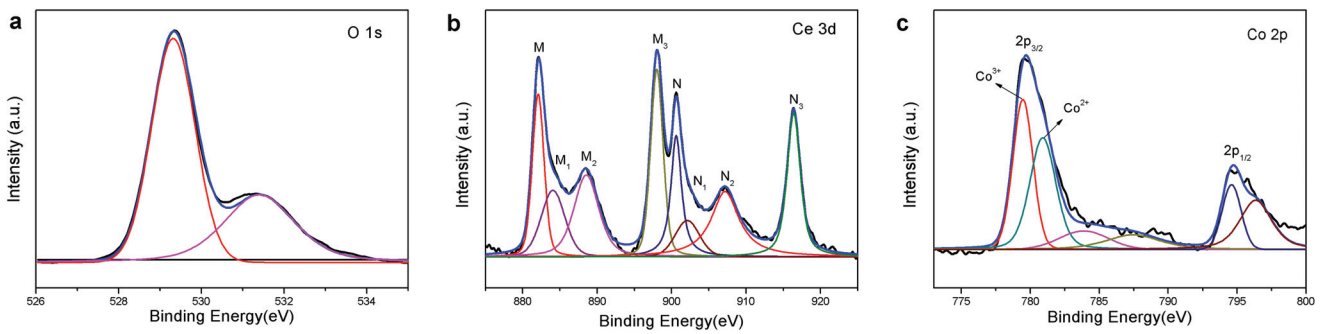

Fig. 3 XPS spectra of the as-prepared porous CeO_2/Co_3O_4 nanojunctions: (a) O 1s binding energy spectrum, (b) Ce 3d binding energy spectrum, (c) Co 2p binding energy spectrum.

This journal is © The Royal Society of Chemistry 2016

Published on 07 November 2016. Downloaded by University of Science and Technology of China on 14/06/2017 03:17:43.

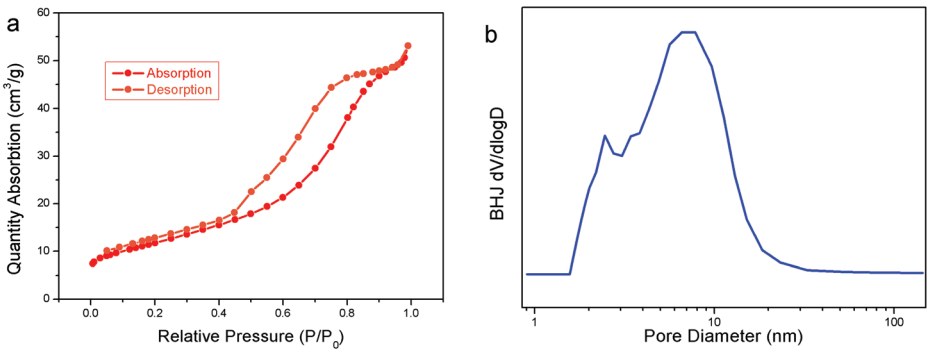

Fig. 4 (a) Nitrogen adsorption/desorption isotherm at 77 K for porous CeO_2/Co_3O_4 nanojunctions (b) the pore size distribution calculated using the BJH equation from N_2 adsorption.

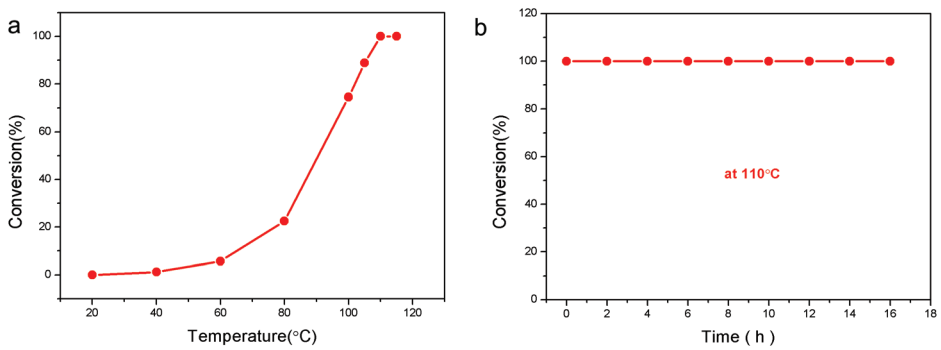

Fig. 5 (a) Conversion as a function of temperature for CO oxidation over porous CeO_2/Co_3O_4 nanojunctions, (b) stability of porous CeO_2/Co_3O_4 nanojunctions at the temperature of 110 °C.

junctions.[37,38] And this interaction is further demonstrated in Fig. 6a.

To further investigate the specific surface area and the porous nature of the as-prepared CeO_2/Co_3O_4 nanojunctions, Brunauer–Emmett–Teller(BET) gas sorption measurements were performed. Fig. 4a shows the N_2 adsorption/desorption isotherm of porous CeO_2/Co_3O_4 nanojunctions. The isotherm is identified as type IV, which is characteristic of mesoporous materials. The sample is found to have a moderate BET specific surface area of 42.3 $m^2\ g^{-1}$. The pore size distribution obtained from the isotherm is shown in Fig. 4b. According to the Barrett–Joyner–Halenda (BJH) method, the average pore size of porous CeO_2/Co_3O_4 nanojunctions is calculated as 7.8 nm. These pores presumably arise from the release of gaseous molecules (*e.g.* CO_2 and H_2O) during the annealing process. And these nanopores can provide paths for gas diffusion, which are beneficial for CO catalytic oxidation.

As a typical probe reaction of many novel catalytic materials,[39] CO oxidation is carried out to evaluate the catalytic activities of the prepared nanojunction structures. T_{100}, the temperature for 100% CO oxidation, is used to evaluate the catalytic performance of the sample. To make a comparison, we also test the catalytic performance of pure Co_3O_4 for CO oxidation. The detailed synthesis method for Co_3O_4 can be seen in the ESI.† Other instrumental analyses such as SEM, TEM (Fig. S6†) and XRD (Fig. S7 and S8†) were also used to characterize the structure of the as-prepared $Co_3[Co(CN)_6]_2$ and Co_3O_4. Fig. 5a shows the curves of CO conversion as a function of temperature for the prepared sample. As we can see from Fig. 5a, CO undergoes complete conversion at a low temperature of 110 °C for porous CeO_2/Co_3O_4 nanojunctions, while the T_{100} is as high as 190 °C for pure Co_3O_4 (Fig. S10†). We also compared our material with similar catalysts in the previous literature (Table S1†). From the table, it could be found that catalytic activity of our material is superior to those of the reported catalysts, and even better than the performance of some noble metal-based catalysts (Table S2†). What is more, the high activity of porous CeO_2/Co_3O_4 nanojunctions can be maintained after 16 h (Fig. 5b) without any decline, which indicates that our material has excellent catalytic stability.

For a further evaluation of their catalytic stability, we also characterized the porous CeO_2/Co_3O_4 nanojunctions after the CO oxidation test by TEM and XRD analyses. Fig. S11† is the TEM image of porous CeO_2/Co_3O_4 nanojunctions after the CO oxidation test. It is obviously seen that the hexagonal morphology of porous CeO_2/Co_3O_4 nanojunctions is retained quite well. The XRD patterns of porous CeO_2/Co_3O_4 nanojunctions after the CO oxidation test are shown in Fig. S12.† There is no clear difference in the XRD results before and after the CO oxidation test, which indicates that the porous CeO_2/Co_3O_4 nano-

Published on 07 November 2016. Downloaded by University of Science and Technology of China on 14/06/2017 03:17:43.

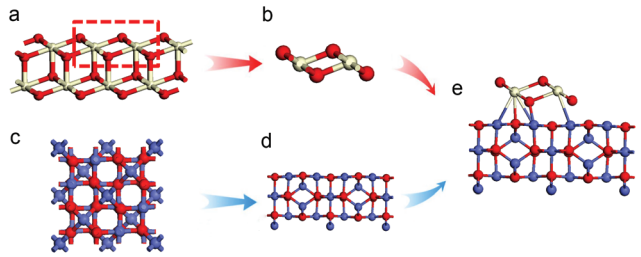

Scheme 2 The scheme for the model construction of the CeO_2–Co_3O_4 interface, (a) model of CeO_2, (b) model of CeO_2 (111), (c) model of Co_3O_4, (d) model of Co_3O_4 (110), (e) model of the CeO_2–Co_3O_4 interface.

junctions are sufficiently stable during the catalytic CO oxidation process.

In order to gain further insights into the effect of the interface towards CO catalytic oxidation, we carried out density functional theory calculations. The model for the CeO_2–Co_3O_4 interface was constructed as shown in Scheme 2. Our calculation results show that CeO_2 has a strong interaction with Co_3O_4. As shown in Fig. 6a, a strong electron coupling effect has been observed at the interface between CeO_2 and Co_3O_4. The difference between the work functions of these two materials drives the charge transfer through the interface, which may alter catalytic reactivity of CO catalytic oxidation.

As the adsorption process is essential and taken as the starting step for many chemical reactions, we carried out theoretical calculations of the adsorption energy of CO on the interface of CeO_2/Co_3O_4. In addition, CO on the surface of pure CeO_2 and pure Co_3O_4 was also calculated for comparison. The calculation results show that CO interacts weakly with the (111) ceria surface. As shown in Fig. 7a, the CO molecule adsorbs on the top of the Ce atom with the carbon end towards the (111) ceria surface and the molecular axis parallel to the surface normal direction. The C atom lies at 2.846 Å above the surface of the Ce atom. The calculated adsorption energy is −0.176 eV (Fig. 7d), which agrees with the result of the previous theoretical study −0.170 eV.[40] This indicates that CO physisorbs on the (111) ceria surface, consistent with Berner *et al.*[41] Experimental results suggest that the interaction between CO and unreduced CeO_2 (111) is very weak. However, CO is found to form strong chemical bonds with the Co_3O_4 (110) surface. As depicted in Fig. 7b, the CO molecule adsorbs with the carbon pointing toward the Co_3O_4 (110) surface as it binds to the Co^{3+} site. The C atom is at the top of the Co atom with a distance of 1.768 Å. At the same time, the C–O bond has greatly been elongated from 1.143 to 1.155 Å, which is characteristic of an activated molecule. Obviously, CO interacts strongly with the Co_3O_4 (110) surface. And the adsorption energy is −1.203 eV, which is in agreement with the result of previous theoretical investigation,[42] indicating that CO strongly chemisorbs on the Co_3O_4 (110) surface.

Interestingly, CO adsorbed on the interface of CeO_2/Co_3O_4 has a similar characteristic to that adsorbed on the Co_3O_4 (110) surface. But the molecule–interface interaction is not as strong as the interaction of CO with the Co_3O_4 (110) surface. The adsorption energy is −1.13 eV, which is lower than that on

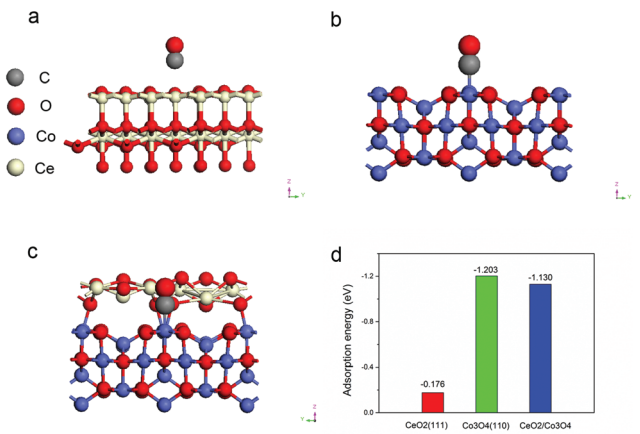

Fig. 7 (a–c) Schematic structure of CO adsorbed on the (111) ceria surface, the Co_3O_4 (110) surface and the interface of CeO_2/Co_3O_4, respectively. (d) Calculated adsorption energy (in eV) for the CO molecule on CeO_2 (111), Co_3O_4 (110) and CeO_2/Co_3O_4 surfaces.

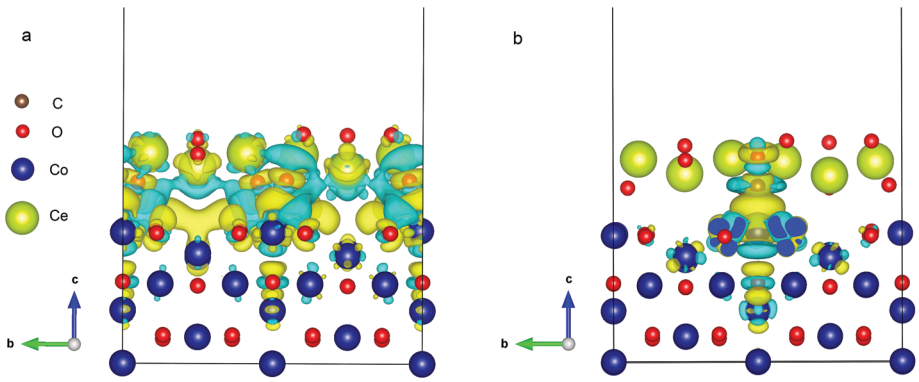

Fig. 6 (a) Charge-density difference of the CeO_2–Co_3O_4 interface, (b) charge-density difference of the CO molecule adsorbed on the CeO_2–Co_3O_4 interface. Olive color and cyan color illustrate the increase and decrease of electron distributions.

This journal is © The Royal Society of Chemistry 2016

Published on 07 November 2016. Downloaded by University of Science and Technology of China on 14/06/2017 03:17:43.

the Co_3O_4 (110) surface. According to the Sabatier principle, a general explanatory paradigm in heterogeneous catalysis, optimal catalytic activity can be achieved on a catalytic surface with intermediate adsorption energies for reactive molecules.[43] The CO molecule absorbs too weakly on the (111) ceria surface, so it is difficult for the ceria surface to activate it. While the adsorption of the CO molecule on the Co_3O_4 (110) surface is extremely strong, and thus it will occupy all available surface sites and poison the reaction. The adsorption energy of the CO molecule on the interface of CeO_2/Co_3O_4 permits a compromise between these two materials. That's why porous CeO_2/Co_3O_4 nanojunctions show an enhancement of catalytic activity for CO catalytic oxidation.

As the activation of dioxygen is also an important step in the CO oxidation reaction,[44] we further calculate the adsorption of O_2 on pure Co_3O_4 and the interface of CeO_2/Co_3O_4 nanojunctions. The optimized structures of adsorbed dioxygen species are depicted in Fig. S13.† As our calculations show, the adsorption configurations are end-on, involving the O_2 molecule axis perpendicular to the surface, which are in good agreement with the previous theoretical study.[45] As seen in Table S3,† the length of the O–O bond has been elongated from 1.236 to 1.282 Å, indicating that the O_2 molecule has been activated by Co_3O_4. Interestingly, the O–O distance of the adsorbed O_2 on the interface of CeO_2/Co_3O_4 nanojunctions is 1.287 Å, which is longer than that of pure Co_3O_4, further enhancing O_2 activation.

Heterogeneous catalysis often involves charge transfer from catalysts to adsorbed molecules, so we also calculated the charge-density difference of the CO molecule adsorbed on the interface of CeO_2/Co_3O_4. As shown in Fig. 6b, there is obviously a charge transfer between the interface and the CO molecule. This phenomenon indicates that the CO molecule has formed a covalent bond with the interface. And this binding is accompanied by a back-donation of electrons from the interface into the $2\pi^*$ antibonding orbital of the CO molecule, making the CO molecule more reactive.

Conclusion

In summary, we report the experimental and theoretical investigations on the catalytic activity of CeO_2/Co_3O_4 nanojunctions for CO oxidation. A novel MOF-annealing strategy was developed to synthesize CeO_2/Co_3O_4 nanojunctions, which exhibited enhanced catalytic performance towards CO oxidation compared with pure Co_3O_4. This outstanding catalytic activity is attributed to their unique nanojunction structure. A large number of interfaces were *in situ* generated in the nanojunctions during the annealing process, which played an importance role in the catalytic CO oxidation reaction. Density functional theory calculations indicated that the charge transferred through the interfaces between Co_3O_4 and CeO_2, altered the behavior of CO absorption on nanojunctions, and tailored the catalytic properties. This work will not only help in the understanding of the role of nanojunctions in catalytic reactions, but also provide insights for future design and development of high performance nanojunction materials.

Acknowledgements

This work was supported by the National Natural Science Foundation (NSFC, 21271163, U1232211), the CAS/SAFEA International Partnership Program for Creative Research Teams and the Hefei Science Center CAS (2016HSC-IU011), and the calculations were completed on the supercomputing system in the Supercomputing Center of USTC.

References

1 B. K. Min and C. M. Friend, *Chem. Rev.*, 2007, **107**, 2709–2724.
2 H. J. Freund, G. Meijer, M. Scheffler, R. Schlögl and M. Wolf, *Angew. Chem., Int. Ed.*, 2011, **50**, 10064–10094.
3 H. Yen, Y. Seo, S. Kaliaguine and F. Kleitz, *Angew. Chem., Int. Ed.*, 2012, **51**, 12032–12035.
4 Y. Zhou, Z. Wang and C. Liu, *Catal. Sci. Technol.*, 2015, **5**, 69–81.
5 M. S. Chen, Y. Cai, Z. Yan, K. K. Gath, S. Axnanda and D. W. Goodman, *Surf. Sci.*, 2007, **601**, 5326–5331.
6 H. Falsig, B. Hvolbæk, I. S. Kristensen, T. Jiang, T. Bligaard, C. H. Christensen and J. K. Nørskov, *Angew. Chem., Int. Ed.*, 2008, **120**, 4913–4917.
7 J. Y. Park, Y. Zhang, M. Grass, T. Zhang and G. A. Somorjai, *Nano Lett.*, 2008, **8**, 673–677.
8 C. Xu, J. Su, X. Xu, P. Liu, H. Zhao, F. Tian and Y. Ding, *J. Am. Chem. Soc.*, 2007, **129**, 42–43.
9 K. Liu, A. Wang and T. Zhang, *ACS Catal.*, 2012, **2**, 1165–1178.
10 Y. Zhang, X. Weng, H. Li, H. Li, M. Wei, J. Xiao, Z. Liu, M. Chen, Q. Fu and X. Bao, *Nano Lett.*, 2015, **15**, 3616–3623.
11 X. Yu and P. G. Pickup, *Electrochem. Commun.*, 2009, **11**, 2012–2014.
12 S. Royer and D. Duprez, *ChemCatChem*, 2011, **3**, 24–65.
13 Y. Ren, Z. Ma, L. Qian, S. Dai, H. He and P. G. Bruce, *Catal. Lett.*, 2009, **131**, 146–154.
14 X. Y. Pang, C. Liu, D. C. Li, C. Q. Lv and G. C. Wang, *ChemPhysChem*, 2013, **14**, 204–212.
15 N. Yan, Q. Chen, F. Wang, Y. Wang, H. Zhong and L. Hu, *J. Mater. Chem. A*, 2013, **1**, 637–643.
16 X. Liu, K. Zhou, L. Wang, B. Wang and Y. Li, *J. Am. Chem. Soc.*, 2009, **131**, 3140–3141.
17 J. Shi, *Chem. Rev.*, 2013, **113**, 2139–2181.
18 Q. Fu, W. X. Li, Y. X. Yao, H. Y. Liu, H. Y. Su, D. Ma, X. K. Gu, L. M. Chen, Z. Wang, H. Zhang, B. Wang and X. H. Bao, *Science*, 2010, **328**, 1141–1144.
19 G. Chen, Y. Zhao, G. Fu, P. N. Duchesne, L. Gu, Y. Zheng, X. Weng, M. Chen, P. Zhang, C. W. Pao, J. F. Lee and N. Zheng, *Science*, 2014, **344**, 495–499.

Published on 07 November 2016. Downloaded by University of Science and Technology of China on 14/06/2017 03:17:43.

20 Y. Bai, W. Zhang, Z. Zhang, J. Zhou, X. Wang, C. Wang, W. Huang, J. Jiang and Y. Xiong, *J. Am. Chem. Soc.*, 2014, **136**, 14650–14653.
21 S. T. Kochuveedu, Y. H. Jang and D. H. Kim, *Chem. Soc. Rev.*, 2013, **42**, 8467–8493.
22 B. Liu, H. Shioyama, T. Akita and Q. Xu, *J. Am. Chem. Soc.*, 2008, **130**, 5390–5391.
23 L. Zhang, H. B. Wu and X. W. Lou, *J. Am. Chem. Soc.*, 2013, **135**, 10664–10672.
24 J. K. Sun and Q. Xu, *Energy Environ. Sci.*, 2014, **7**, 2071–2100.
25 Y. Zhang, Y. Zhou, Y. Zhao and C. j. Liu, *Catal. Today*, 2016, **263**, 61–68.
26 B. Liu, H. Shioyama, T. Akita and Q. Xu, *J. Am. Chem. Soc.*, 2008, **130**, 5390–5391.
27 N. L. Torad, M. Hu, S. Ishihara, H. Sukegawa, A. A. Belik, M. Imura, K. Ariga, Y. Sakka and Y. Yamauchi, *Small*, 2014, **10**, 2096–2107.
28 L. Zhang, H. B. Wu, S. Madhavi, H. H. Hng and X. W. Lou, *J. Am. Chem. Soc.*, 2012, **134**, 17388–17391.
29 Y. Yang, Z. Lun, G. Xia, F. Zheng, M. He and Q. Chen, *Energy Environ. Sci.*, 2015, **8**, 3563–3571.
30 F. Zheng, Y. Yang and Q. Chen, *Nat. Commun.*, 2014, **5**, 5261.
31 F. Zheng, G. Xia, Y. Yang and Q. Chen, *Nanoscale*, 2015, **7**, 9637–9645.
32 R. Zhang, L. Hu, S. Bao, R. Li, L. Gao, R. Li and Q. Chen, *J. Mater. Chem. A*, 2016, **4**, 8412–8420.
33 D. Mullica, W. Milligan and W. Kouba, *J. Inorg. Nucl. Chem.*, 1979, **41**, 967–973.
34 C. Yuan, J. Li, L. Hou, X. Zhang, L. Shen and X. W. D. Lou, *Adv. Funct. Mater.*, 2012, **22**, 4592–4597.
35 F. Zheng, D. Zhu, X. Shi and Q. Chen, *J. Mater. Chem. A*, 2015, **3**, 2815–2824.
36 P. Burroughs, A. Hamnett, A. F. Orchard and G. Thornton, *J. Chem. Soc., Dalton Trans.*, 1976, 1686–1698.
37 P. K. Babu, A. Lewera, J. H. Chung, R. Hunger, W. Jaegermann, N. Alonso-Vante, A. Wieckowski and E. Oldfield, *J. Am. Chem. Soc.*, 2007, **129**, 15140–15141.
38 J. Wang, K. Li, H. x. Zhong, D. Xu, Z. l. Wang, Z. Jiang, Z. j. Wu and X. b. Zhang, *Angew. Chem., Int. Ed.*, 2015, **54**, 10530–10534.
39 H. Bao, W. Zhang, Q. Hua, Z. Jiang, J. Yang and W. Huang, *Angew. Chem., Int. Ed.*, 2011, **50**, 12294–12298.
40 Z. Yang, T. K. Woo and K. Hermansson, *Chem. Phys. Lett.*, 2004, **396**, 384–392.
41 U. Berner, K. Schierbaum, G. Jones, P. Wincott, S. Haq and G. Thornton, *Surf. Sci.*, 2000, **467**, 201–213.
42 P. Broqvist, I. Panas and H. Persson, *J. Catal.*, 2002, **210**, 198–206.
43 P. Sabatier, *Ber. Dtsch. Chem. Ges.*, 1911, **44**, 1984–2001.
44 Y. Lou, J. Ma, X. Cao, L. Wang, Q. Dai, Z. Zhao, Y. Cai, W. Zhan, Y. Guo, P. Hu, G. Lu and Y. Guo, *ACS Catal.*, 2014, **4**, 4143–4152.
45 X. L. Xu, E. Yang, J. Q. Li, Y. Li and W. K. Chen, *ChemCatChem*, 2009, **1**, 384–392.

This journal is © The Royal Society of Chemistry 2016